Available online at www.sciencedirect.com
jmr&t
Journal of Materials Research and Technology
journal homepage: www.elsevier.com/locate/jmrt

Original Article

Effects of tangential supersonic airflow on the laser ablation of laminated CFRP

Weina Zhao [a,b,d,1], Te Ma [a,b,1], Hongwei Song [a,b,c,*], Wu Yuan [a,b],
Ruixing Wang [a,b], Zhe Wang [a,b], Lingling Lu [a,b], Chenguang Huang [b]

[a] Key Laboratory for Mechanics in Fluid Solid Coupling Systems, Institute of Mechanics, Chinese Academy of Science, Beijing 100190, China
[b] School of Engineering Science, University of Chinese Academy of Sciences, Beijing 100049, China
[c] State Key Laboratory of High Temperature Gas Dynamics, Institute of Mechanics, Chinese Academy of Science, Beijing 100190, China
[d] School of Science, Qingdao University of Technology, Qingdao 266520, China

ARTICLE INFO

Article history:
Received 24 March 2021
Accepted 21 July 2021
Available online 24 July 2021

Keywords:
Laminated CFRP
Laser ablation
Mechanical erosion
Supersonic wind tunnel

ABSTRACT

Ablation behaviors of laminated carbon fiber reinforced plastics (CFRP) subjected to intense continuous wave laser in the supersonic wind tunnel are investigated experimentally. Comparable laser ablation tests in other environments, i.e., static air, static nitrogen and open airflow, are also carried out. Laser ablation rate in the supersonic wind tunnel is significantly larger than those of the other environments, in particular, at least twice of that in an open tangential airflow condition. The ablation morphology can be classified into two regions, coupled ablation zone (CAZ) and downstream affected zone (DAZ). Coupled thermal-fluid-solid analysis including thermochemical ablation and thermomechanical erosion models reveals that the contribution of each laser mechanisms is distinctive at the different positions of the laser ablation pit.

1. Introduction

Carbon fiber reinforced plastics (CFRP) have been increasingly used in various industrial sectors, due to exceptional characteristics such as light weight, high specific strength, high specific stiffness, improved chemical resistance, tailorable shock and thermal resistance. In particular, CFRP have been closely related to aerospace structures, because of high–performance combination and weight saving demands in this type of application [1–4]. When subjected to high thermal loadings or streamlined with high-temperature/high-speed gas flows, the mechanisms of thermal-chemical-physical destruction of CFRP materials are very complex [5,6]. The chemical process mainly involves decomposition and gasification of the polymer matrix and carbon fibers, oxidation of residual char and carbon fibers. The physical process mostly includes phase transitions of evaporation or sublimation, thermal expansion and contraction, thermal-induced strains, fiber-matrix interfacial debonding, matrix cracking, delamination damage and mechanical erosion [7–9]. Therefore, the thermal-mechanical behavior and ablation performance of CFRP are illusive to model.

---

[*] Corresponding author.
E-mail address: songhw@imech.ac.cn (H. Song).
[1] These authors contributed to the work equally and should be regarded as co-first authors.

https://doi.org/10.1016/j.jmrt.2021.07.101

It is an interesting and practical topic to investigate thermal-mechanical behaviors and ablation performance of carbon fiber or polymer composites subjected to the intense heat from laser irradiation [10–17]. Kreling et al. [12] performed scanning electron microscopy (SEM) and X-ray photoelectron spectroscopy (XPS) analytical experiments on CFRP surfaces pre-treated with 308 nm excimer laser radiation. Leone et al. [13] demonstrated that there were different mechanisms, such as ablation, matrix burning and mechanical effects, which might affect the laser beam–material interaction in laser machining of CFRP. Dimitrienko et al. [18] studied thermo-mechanical behavior of a polymer composites heated by laser irradiation. The authors observed that interlayer shear, tangential shrinkage stresses and through-thickness tensile stresses are causes of delamination and cracking. Huang et al. [19] found the material mass ablation law of the carbon fiber epoxy composite irradiated by continuous laser experimentally. In their work, the composite ablation mass is proportional to the laser radiation energy density when the laser radiation intensity is greater than 10 kW/cm^2. Besides, when the laser radiation intensity is near the composite burning threshold, the combustion phenomena cause the fluctuation of mass ablation rate. Tong et al. [20] proposed ablation mechanisms of different regions to describe the ablation behavior of C/SiC composites irradiated by a pulsed laser. Chippendale et al. [21] modeled thermo-chemical degradation of carbon fiber composite (CFC) materials under intensive heat fluxes. The authors considered heat diffusion, polymer pyrolysis associated with gas production and convection through partially decomposed CFCs, and changes in transport properties of the material due to the damage. Mucha et al. [22] used a one-dimensional heat flow model to investigate the extent of matrix damage zones observed by experiments. The results revealed that the extents of the matrix damage zones are dominated by a total interaction time, which includes the passage of the laser beam and the continued interaction of the cloud of hot ablation products with the carbon fibers at the kerf wall. Wu et al. [23] studied ablation behaviors of CFRP laminates by laser of different operation modes. Results revealed that the continuous wave laser made constant ablation of epoxy matrix over several layers, and the long duration pulsed wave laser made conical hole through the total laminate thickness. Salama et al. [24] analyzed the effects of laser processing parameters (e.g. laser power, scanning speed and repetition rate) on heat-affected zone (HAZ) sizes and ablation depth of CFRP composites, using a state-of-the-art 400 W ps laser system.

In spite of many researches on laser ablation, the exact mechanisms of laser ablation on carbon fiber composites (e.g. thermal vs. mechanical effects) are not yet fully understood. Moreover, different kinds of mechanisms can play a role, depending on the type of material, laser parameters, gas environment [25]. Among them, high-speed airflow and mechanical erosion may strongly affect the laser ablation behavior. Farhan et al. [26] studied the effects of density and fiber orientation on the ablation behavior of carbon–carbon composites, and found that fibers were easily turned into a sharp wedge shape when subjected to the erosion from the oxy-acetylene flame having an angle of 30° with respect to the fibers. Zhang et al. [27] studied the influence of tangential airflows velocity at low subsonic and laser intensity on laser ablation heat of glass fiber reinforced epoxy composites. Results showed that, when the laser intensity was below 200 W/cm^2, laser ablation increased with the airflow velocity on the same laser irradiation. Helber et al. [28] investigated the resistance of carbon-phenolic ablators AQ61 and Asterm to high heating conditions in air and nitrogen plasmas, and characterized gas–surface interaction phenomena, including the interaction of the pyrolysis gases with the hot plasma flow. Peng et al. [29] developed a model and criterion for simulating mechanical erosion process on laser irradiating glass/epoxy composite. In the model, a thermo-mechanical model was used before composite delamination, while plates and shell theory was used for simulating layer fracture. Lachaud et al. [30,31] proposed a chemical equilibrium heat and mass transport model to analyze the boundary layer and pyrolysis gas flows in porous ablative materials. Tangential airflow increases ablative rate by removing ablation products and reduces the burn-through time. The high-speed airflow also eliminates the oxidation products and supplies extra oxygen. However, most of previous studies of laser ablation are conducted in conventional experimental environment, for instance, static test conditions or low-speed airflow. To the best knowledge of the authors, there are no experimental data available for the laser ablation behavior of laminated CFRP in a supersonic wind tunnel environment. Moreover, there is no direct experimental data to compare laser ablation behaviors of CFRP composites under different environments.

In the present study, laser irradiation experiments of laminated CFRP in a supersonic wind tunnel are carried out, in addition to several conventional environments, including static air, static nitrogen and open airflow. Laser ablation mechanisms and ablation rates in different environments are discussed and compared. Simulations for laser ablation are not yet state of the art, due to the complexity of ablation processes where a variety of different chemical-physical phenomena are coupled with each other [32–34]. Despite the difficulties, a coupled fluid-solid thermal ablation model is established to simulate the laser ablation behaviors of laminated CFRP, and effects of thermochemical ablation and thermomechanical erosion are discussed.

2. Experiments

2.1. Specimen preparation

Laminated T700/BA9916 CFRP plates with the ply pattern of $[45°/0°/\text{-}45°/90°]_{2S}$ are fabricated and provided by AVIC Composite Corporation Ltd. The curing temperature for BA9916 epoxy is 180 °C, as shown in Fig. 1. During preparation, prepreg tapes are heated to 180 °C at the rate of 0.3–3 °C/min, and kept in this specific temperature for 180 min, then dropped to the room temperature (RT) at the maximum rate of 2 °C/min. The curing pressure is 0.6 MPa. Mechanical and physical properties of unidirectional prepreg tapes are shown in Table 1. The initial fiber volume fraction is $\phi_f = 0.533$. Samples are tailored in dimensions of 50 × 50 × 2.4 mm, and the lamina thickness is 0.15 mm.

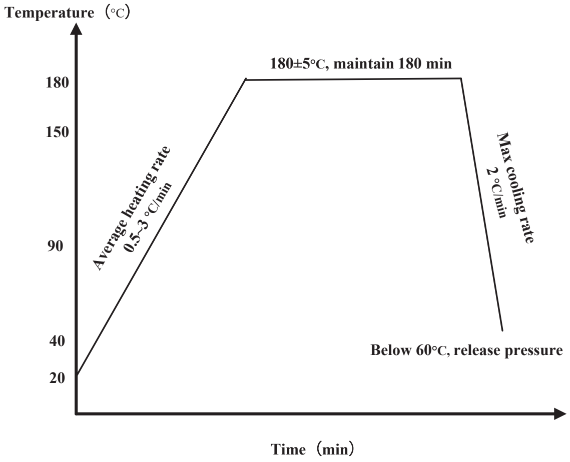

Fig. 1 – Curing of T700/BA9916 composites.

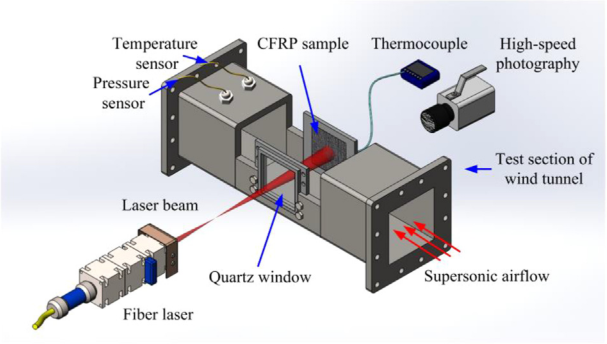

Fig. 2 – Experimental setup for laser ablation in the supersonic wind tunnel.

2.2. *Experimental procedure*

The main objective of the experiment is to investigate the effect of tangential supersonic airflow on laser ablation behaviors of CFRP, and compare ablation mechanisms and ablation rates with other environments.

The experimental setup of laser ablation in the supersonic wind tunnel is shown in Fig. 2. The supersonic wind tunnel facility in the State Key Laboratory of High Temperature Gas Dynamics (LHD) of Institute of Mechanics, Chinese Academy of Sciences, is employed in the experiment. It is based on the principle of oxygen-hydrogen combustion, and can provide a free-stream of Mach 1.8 to 4 in the test section. The CFRP sample is placed in the test section with a specially designed fixture, which guarantees a tangential flow of the supersonic free-stream over one side of the specimen. This side is also subjected to laser irradiation during the test. The laser beam irradiated upon the CFRP sample through a high temperature quartz window. An IPG YLS fiber laser working at 1070 nm wavelength is employed in the present study. The other side of the specimen is installed with a thermocouple and recorded by a high-speed camera. It is worth mentioning that a pressure sensor and a temperature sensor are installed at the test section of wind tunnel to real-time observe the total pressure and original temperature data, respectively.

Experimental parameters for wind tunnel test under different freestream Mach number can be obtained from the aerodynamic functions

$$\begin{aligned} \frac{P}{P_0} &= \left(1+\frac{\gamma-1}{2}M^2\right)^{-\frac{\gamma}{\gamma-1}} \\ \frac{T}{T_0} &= \left(1+\frac{\gamma-1}{2}M^2\right)^{-1} \end{aligned} \tag{1}$$

where P and P_0 are static pressure and total pressure, T and T_0 are static temperature and total temperature, M is Mach number, γ is ratio of specific heat that is defined as the ratio of specific heat at constant pressure to specific heat at constant volume. In consideration of practical applications, it is assumed that these parameters are based on the 20 km altitude service environment: the static pressure $P = 5.46$ kPa, static temperature $T = 220$ K. The static temperature 220 K is estimated by the temperature dropping rule of the troposphere. Using the ground surface temperature as the reference, the air temperature decreases by 6.5 K Celsius per 1 km upward. According to the gas dynamics, for air, the value of the ratio of specific heat γ can be set as 1.4. Experimental parameters can be obtained according to Eq. (1): when Mach number is set to 1.8, the total temperature is 363 K, and total pressure is 0.323 MPa; When Mach number is set to 3.0, the total temperature is 815 K, and total pressure is 1.85 MPa.

Tested parameters for Mach 1.8 and Mach 3.0 are shown in Fig. 3, which basically agree with preset parameters. The detailed real-time data of temperature and pressure are

Table 1 – The main mechanical and physical properties of the T700/BA9916 prepreg tapes.

Mechanical Properties (Room temperature)	Parameter	Physical Properties (Room temperature)	Parameter
0°Tensile Strength (MPa)	1489	Epoxy content (wt%)	38 ± 3
0°Tensile Modulus (GPa)	132.8	Epoxy density (g/cm^3)	1.3 ± 0.04
90°Tensile Strength (MPa)	58.5	Carbon fiber density (g/cm^3)	1.78 ± 0.04
90°Tensile Modulus (GPa)	9.7	Volatile content (%)	≤1.5
0°Compressive Strength (MPa)	1005	Epoxy flow content (%)	5–20
0°Compressive Modulus (GPa)	119.8	Porosity (%)	≤1.5
90°Compressive Strength (MPa)	200	lamina thickness (mm)	0.15 ± 0.015
90°Compressive Modulus (GPa)	9.8		
Shear Strength (MPa)	121		
Shear Modulus (GPa)	5.3		

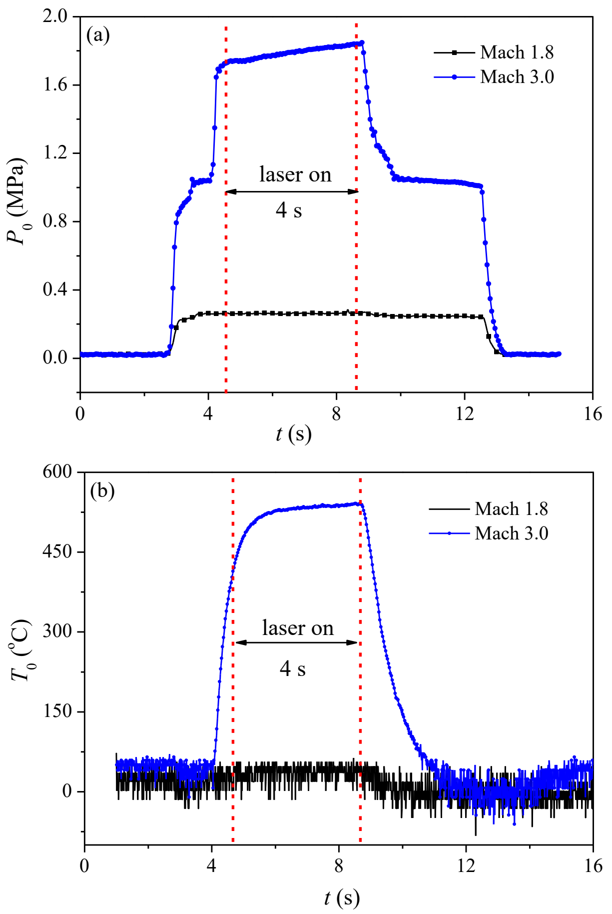

Fig. 3 – Experimental parameters in wind tunnel tests for Mach 1.8 and Mach 3.0 (a) total pressure, (b) total temperature.

measured by sensors equipped in the test cabin of wind tunnel. When the total pressure and total temperature of the freestream is nearly stable, the fiber laser is switched on. The flat head laser beam to the target is 10 mm in diameter, and irradiated for 4 s. The output laser power is set as 1000 and 2000 W for both Mach 1.8 and Mach 3.0 tests, respectively.

To compare with ablation behaviors of CFRP composites in supersonic wind tunnel tests, 3 other types of laser ablation tests were also carried out in different environments, i.e., tangential airflow in an open environment (simplified as “open airflow”), static air environment and static nitrogen environment. The output laser power is also set as 1000 and 2000 W. A Mach 2 nozzle is designed for the open airflow tests, and the total temperature is RT. It should be noted that open airflow is not a strictly ideal experimental condition: it can hardly provide a constant test section, since it lacks suction devices; and the static temperature is well below zero, since the internal energy of pressured gas at RT is converted to kinetic energy upon release. Nevertheless, open airflow has been widely adopted due to the ease of implementation.

It is natural to expect that distinctive ablation patterns would arise in the specimens under different environments. For instance, when CFRP laminates are irradiated by laser in the air environment, matrix decomposition, oxidation of carbon and fiber sublimation may take place, whereas oxidation does not occur in nitrogen environment. However, up to now there are no parallel experimental data available to compare the ablation behaviors directly or quantitatively.

2.3. *Ablation behaviors*

After tests, the HIROX three-dimensional microscope (KH-8700) and scanning electron microscopy (SEM) were used to observe the ablation behaviors, including ablation morphologies, ablation depth and ablation volume. The ablation rate, defined as the ratio of mass loss to virgin mass of laser beam covered zone (10 mm in diameter), can be also derived. In this paper, the ablation degree is evaluated individually by the ablative zone, the ablation depth and the ablative mass. To be more specific, the ablative zone is measured by the longitudinal and transversal dimensions of the surficial ablation zone. The ablation depth is defined as the maximum depth of ablation pit with respect to the origin surface. The ablation volume is the volume of the ablation pit.

Figs. 4 and 5 are ablation morphologies of CFRP laminates irradiated by laser power of 1000 and 2000 W respectively, corresponding to power density of 1274 and 2548 W/cm^2. From Fig. 4a and b as well as Fig. 5a and b, it is seen that in wind tunnel tests the surface carbon fiber fabric has been elliptically cut and relative complex morphology appears around the edge region, but the carbon fibers have not been completely ablated even though several layers of epoxy have been removed by laser irradiation. Since the decomposition of epoxy matrix brings away much of the incident laser energy, the temperature of irradiated carbon fibers is typically below the sublimation point. The dimension of ablation area in longitudinal direction (the direction of airflow) is nearly thrice of the radius of laser beam, mainly dues to the thermomechanical effect caused by the tangential supersonic airflow. For the specific case where the total temperature of the airflow is about 815 K and the Mach is 3.0, the thermomechanical erosion effect plays a much more important role. Comparison of 3D morphologies and cross-sectional ablation depths in different environments also indicates that the supersonic airflow in wind tunnel has prominent influence on the ablation behavior, especially in cases of laser power 2000 W. In Fig. 5a and b, it is found that ablation pits are smoother than those of the other conditions, due to the mechanical erosion effect of supersonic airflow. In Fig. 5c, d and e, the cross-sectional ablation depth fluctuates violently. Moreover, the average ablation depth in wind tunnel tests is larger than that of in the other conditions. Figs. 4c and 5c show that the open airflow has little effect on the morphology of the ablation region. Comparison of Fig. 4d and e, and Fig. 5d and e, it is shown that the affected ablation region in the static air environment is larger than that in the static nitrogen environment, dues to additional oxidation and combustion process in the static air environment. In the nitrogen environment, when the power density is small, only epoxy in the first layers is ablated, leaving bare fibers in the free surface. Therefore, the ablation pit is shallow, and cross-sectional ablation line fluctuates, see Fig. 4e.

For samples tested in the wind tunnel, the ablation area can be divided into two regions: coupled ablation zone (CAZ)

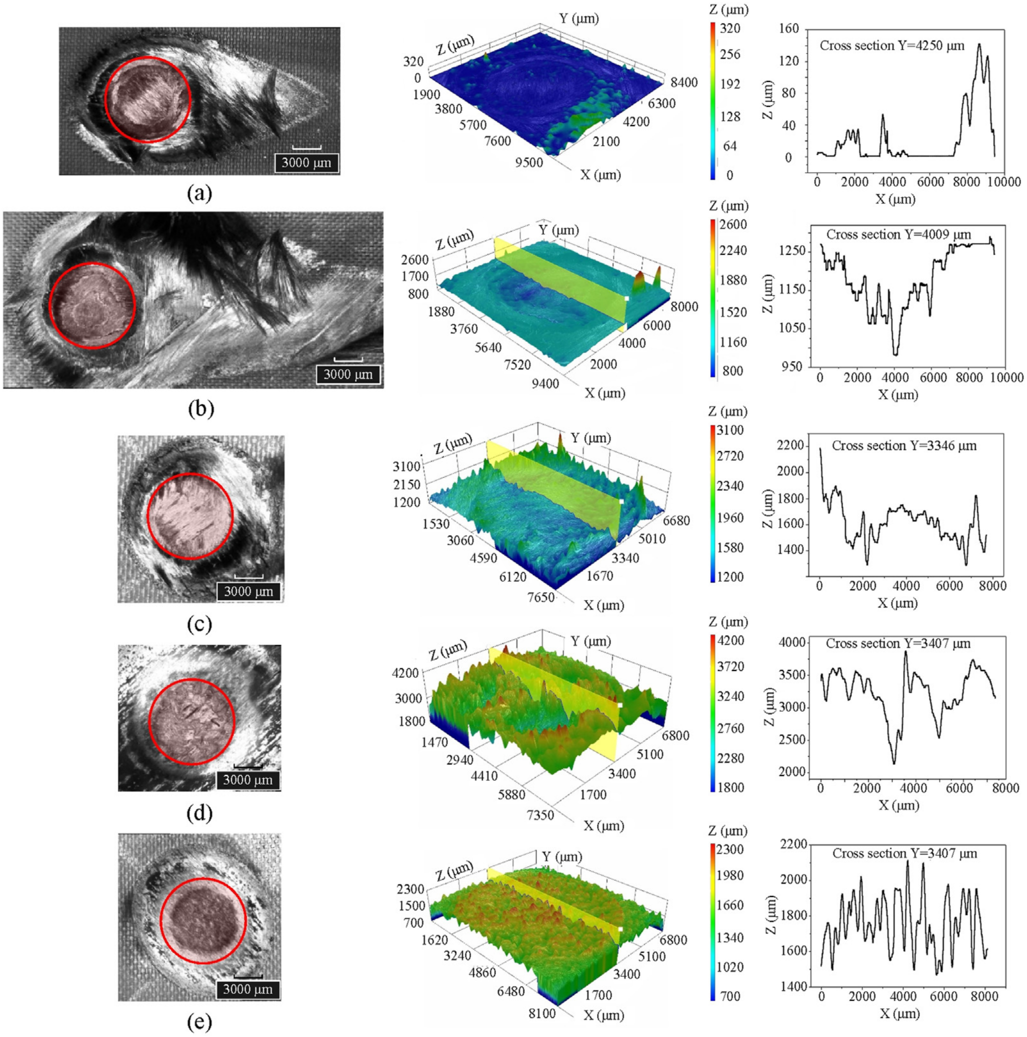

Fig. 4 – Ablation morphologies irradiated by laser power 1000 W (power density 1274 W/cm²), from left to right: surface morphology, 3D morphology and cross-sectional ablation depth (a) wind tunnel of Mach 1.8, (b) wind tunnel of Mach 3.0, (c) open airflow, (d) static air, and (e) static nitrogen. Here, the red circle depicts the main laser beam area that contributes 90% to the total energy.

and downstream affected zone (DAZ), as shown in Fig. 6. In the former, the ablation boundary degradation is mainly caused by the thermo-chemical effect due to laser and the mechanical erosion effect due to high-speed airflow. By contrast, there is no direct laser action on the tail-shape DAZ. The static pressure acting on the edge behind the ablation pit (i.e. the demarcation line between the two regions in Fig. 6) gradually increases with the enlarged ablation depth in CAZ, till it can break the fibers. Meanwhile, the ablated hot products heat up the surface at downstream and induce surface matrix pyrolysis. Since the matrix pyrolysis is surficial, and most of the broken fibers are still attached to the test sample. Comparison of Fig. 4a and b, and Fig. 5a and b, it is also found that the higher the airflow speed, and the higher the laser power density, the longer of the DAZ tail.

Quantitative comparisons of laser ablation behavior are shown in Table 2. Here ablation depth is the maximum depth of ablation pit with respect to the origin surface. Mass loss is readily achieved by measuring of specimen mass before and after experiments. Virgin mass is the mass within laser beam region, which is accounted for 3.15% of the total specimen area (10 mm in diameter of laser beam vs. 50 × 50 mm in dimension of the sample). Ablation rate is one of the most important parameters to calibrate the ablation behavior of CFRP composites, and can be obtained from dividing the mass loss by virgin mass of laser irradiated area.

According to Table 2, laser power density is a key parameter affecting the ablation behavior. Both the ablation depth and ablation rate increase with the laser power density. The ablation rate is less than 100% in normal environment. By contrast, its value can be as high as 166% in wind tunnel environment. This attributes to the strong mechanical erosion effect by supersonic airflow, which accelerates the movement of the ablation front and enlarges the ablation area. As a result, the ablation rate may be larger than 100%. At the same laser power density, the ablation depth and ablation rate are larger in cases of higher Mach number. Comparison of open airflow cases and wind tunnel tests indicates, the mass ablation rate in the wind

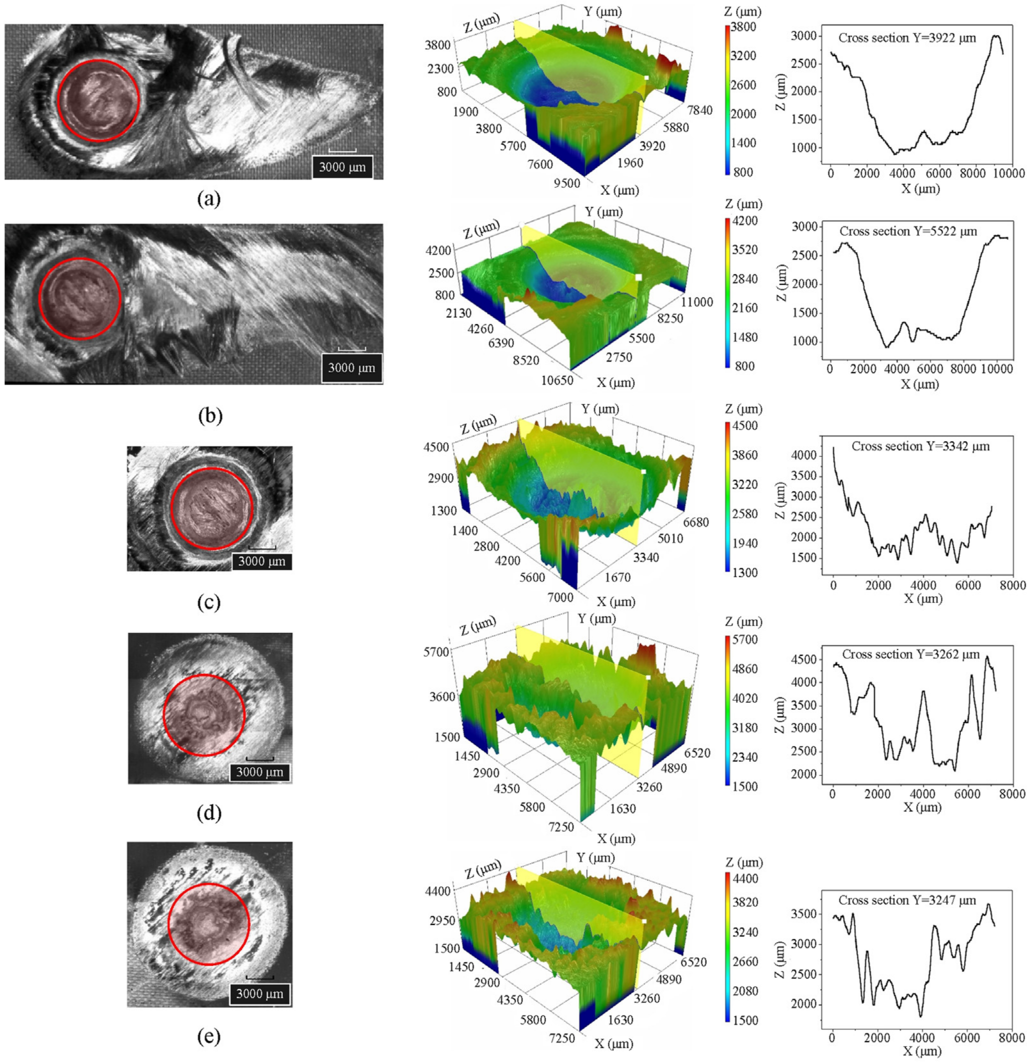

Fig. 5 – Ablation morphologies irradiated by laser power 2000 W (power density 2548 W/cm^2), from left to right: surface morphology, 3D morphology and cross-sectional ablation depth (a) wind tunnel of Mach 1.8, (b) wind tunnel of Mach 3.0, (c) open airflow, (d) static air, and (e) static nitrogen. Here, the red circle depicts the main laser beam area that contributes 90% to the total energy.

tunnel is at least twice that of in open airflow. This means, laser ablation in open airflow, a commonly adopted test method, cannot replace the laser ablation test in the wind tunnel. Table 2 also indicates the laser ablation rate increases in the order of static nitrogen, open airflow, static air, wind tunnel of Mach 1.8 and wind tunnel of Mach 3.0, when compared at the same laser power density.

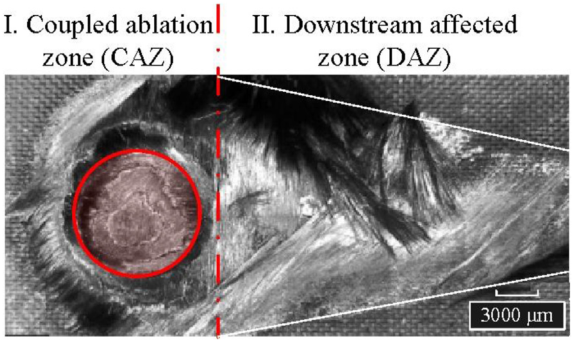

Fig. 6 – The ablation area includes the coupled ablation zone (CAZ) and the downstream affected zone (DAZ).

Fig. 7 gives the SEM view of the ablation region, the sample is from Mach 1.8 wind tunnel with laser power 1000 W. Distinct pyrolysis region and unaffected region can be observed in the image. In the ablation region, epoxy matrix is nearly completely decomposed, leaving bare fibers almost unbundled. The enlarged image of ablation region also shows "needle" shape ablated carbon fibers, indicating sublimation occurs in carbon fibers. The "needle" shape may be sharpened by the supersonic airflow. Multiple delaminations are also observed near the back face opposite to the ablation region. The delamination may occur under the combined action of reactive pressure of pyrolysis gas and thermal stresses.

Table 2 – Quantitative comparisons of laser ablation behaviors.

Environments	Power (W)	power density (W/cm^2)	Ablation depth (μm) Error ± 0.1 μm	Mass loss (g) Error ± 0.001g	Virgin mass (g) Error ± 0.001g	Mass ablation rate (%)
Wind tunnel, Mach 1.8	1000	1274	/	0.288	0.281	102
	2000	2548	1327.6	0.418	0.277	151
Wind tunnel, Mach 3.0	1000	1274	/	0.318	0.280	114
	2000	2548	1565.7	0.458	0.276	166
Open airflow	1000	1274	/	0.070	0.284	24.6
	2000	2548	1340.5	0.210	0.286	73.4
Static air	1000	1274	/	0.090	0.287	31.4
	2000	2548	1202.9	0.250	0.299	83.6
Static nitrogen	1000	1274	/	0.070	0.294	23.8
	2000	2548	1029.4	0.180	0.297	60.6

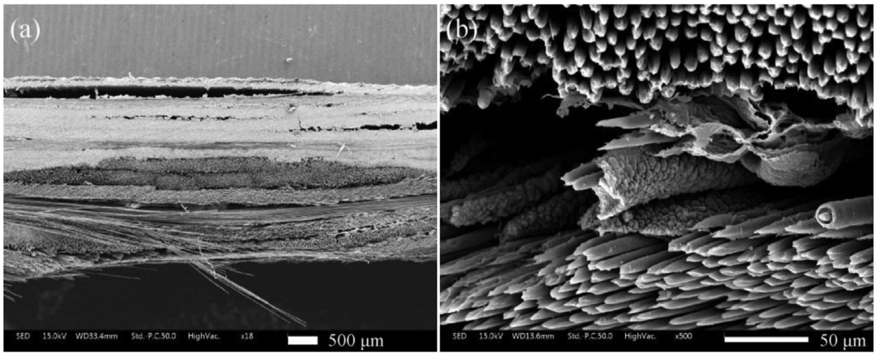

Fig. 7 – SEM view of the ablation region, Mach 1.8 wind tunnel at 1000 W (a) overall view of ablation region, (b) "needle" shape ablated carbon fibers.

3. Modeling laser ablation behavior

3.1. *Thermomechanical model of CFRP*

To model the ablation behavior of laminated CFRP, it is an important step to determinate the thermophysical and thermomechanical properties. These properties are not only temperature dependent but also heating rate dependent, and they are significantly affected by the pyrolysis process. In order to explain the behavior of laser ablation, a complete multi-scale analysis model has been established in our previous work [35]. The irregularly distributed meso-pyrolysis components can be associated with the regularly-distributed mesoscale model through mapping relations to describe the content changes of each component in the pyrolysis process. The pyrolysis kinetics equation of fiber and matrix at high temperature can be expressed using Arrhenius functions [35].

$$\frac{\partial \phi_b}{\partial t} = -J_b \phi_b^n \exp\left(-\frac{E_{Ab}}{RT}\right) \tag{2}$$

$$\frac{\partial \phi_f}{\partial t} = -J_f \left[\phi_f - \phi_f^0 (1 - \Gamma_f)\right]^n \exp\left(-\frac{E_{Af}}{RT}\right) \tag{3}$$

where subscripts f and b represent fiber and matrix, respectively; E_A is the apparent energy of activation; J is the pre-exponential factor; t is the time; Γ_f is the gasification coefficient of fiber. R is the universal gas constant; T is the temperature; n is the reaction order. It should be noted that J, Γ_f, n, and E_A are determined via thermogravimetric analysis (TGA) experiments on the basis of a complete multi-scale analysis model. For detailed explanation, please refer to [35]. Here, the values for these parameters used in this paper are presented at Appendix A.

3.2. *Linear ablation models*

When subjected to high power laser irradiation, high temperature of 1500–3000 °C occurs in the laminated CFRP, linear ablation should be considered into the ablation model. And the total linear rate v_t can be decomposed into oxidation rate v_o, sublimation rate v_s and thermomechanical erosion rate v_m. The equations are listed in Eqs. (4)–(7) [36].

$$v_t = v_o + v_s + v_m \tag{4}$$

$$v_o = \frac{1}{\rho_w} \sum \frac{M_i}{M_{o_2}} p_{o_2 w}^n A_i \exp\left(-\frac{E_{Ai}}{RT_w}\right) \tag{5}$$

$$v_s = \frac{1}{\rho_w} \left(\frac{\alpha}{c_p}\right) \left(\frac{p_g^*}{p_e}\right) \exp\left(-\frac{E_{AS}}{RT_w}\right) \tag{6}$$

$$v_{m\perp} = \frac{1}{\rho_f} \left(\frac{J_f^0 k_f}{c_f}\right)^{1/2} \left(\frac{6p_{\sum}}{\sigma_{f\perp}}\right)^{3/2} \left(\frac{RT_w}{E_{Af}}\right)^{1/2} \exp\left(-\frac{E_{Aft}}{RT_w}\right), v_{m|} = v_{m\perp} \left(\frac{\sigma_{f\perp}}{\sigma_f}\right)^{1/2} \tag{7}$$

where ρ_w is the density of the laminated CFRP; M_i is the average molecular mass of the substance i involved in the oxidation reaction; M_{O2} is the molecular mass of oxygen; p_{o_2w} is the partial pressure of oxygen in the airflow; A_i is the pre-exponential factor of oxidation reaction; α/c_p is the heat transfer coefficient; p_g^* is the gas pressure constant; p_e is the local pressure; is the pressure head of airflow on the ablation surface; σ_f and $\sigma_{f\perp}$ are the strengths of monofibres in the longitudinal and perpendicular directions, respectively.

3.3. Heat balance on the ablative surface

To determine the temperature T_w of laminated CFRP subjected to laser irradiation and tangential airflow, it is necessary to take account of processes of heat and mass transfer occurring on the surface.

Fig. 8 illustrates heat balance on the ablative surface of laminated CFRP.

As shown in Fig. 7, S_{tc} indicates the instantaneous ablation boundary due to thermo-chemical effects, which can be obtained from oxidation rate v_o and sublimation rate v_s. S_{tm} indicates the ablation boundary due to mechanical erosion effects, which can be obtained from thermomechanical erosion rate v_m. And the net conduction heat flux can be obtained from thermal equilibrium in the ablation boundary

$$-\lambda\frac{\partial T}{\partial n}=\alpha q_{\mathrm{laser}}-q_{\mathrm{rad}}-q_{\mathrm{conv}}+q_{\mathrm{oxi}}-q_{\mathrm{deg}}-q_{\mathrm{phas}} \tag{8}$$

where α is absorption coefficient, q_{laser} is the heat flux of laser, q_{rad}, q_{conv}, q_{oxi}, q_{deg}, and q_{phas} are heat flux due to surface radiation, convection between composites and airflow, oxidation of matrix and fiber, decomposition and pyrolysis of composite, and phase change and sublimation, respectively.

According to the radiation law

$$q_{\mathrm{rad}}=\varepsilon\sigma\left(T_{\mathrm{w}}^4-T_0^4\right) \tag{9}$$

where ε is the emissivity of the ablation surface, σ is Stefan–Boltzmann constant, T_{w} is the ablation surface temperature of composite and T_0 is the environment airflow temperature.

According to the Newton's cooling law

$$q_{\mathrm{conv}}=h_w\left(T_{\mathrm{w}}-T_0\right) \tag{10}$$

where h_w is the coefficient of convective heat transfer. Compared with laser heat flux, q_{conv} is at least two orders smaller, and can be neglected in this analysis.

Heat flux due to pyrolysis degradation is

$$q_{\mathrm{deg}}=Q_0\frac{\partial m}{\partial t}-V\left(\phi_g\rho_g\overrightarrow{v}_g\right)\cdot\nabla h_g \tag{11}$$

$$h_g=\int_{T_0}^{T}\rho_g c_g dT=\rho_g c_g\left(T-T_0\right) \tag{12}$$

where Q_0 is the endothermic heat of degradation from the unit mass of the composite. The second part is the convective heat taken away by pyrolysis gas. V is the volume of the composite, h_g is the enthalpy of the pyrolysis gas, ρ_g is the density of the pyrolysis gas, $\overrightarrow{v}_g$ is the velocity vector of the gas flow, c_g is the specific heat of the pyrolysis gas.

For the heat flux due to oxidization q_{oxi}, there are the following oxidization reactions

$$\begin{aligned}&2C+O_2=2CO\\&C+O_2=CO_2\\&C+CO_2=2CO\end{aligned} \tag{13}$$

Heat flux due to oxidization is therefore obtained by counting the heat generation of a global reaction.

$$q_{\mathrm{oxi}}=C_{bef}\Delta H_{bef}-C_{aft}\Delta H_{aft} \tag{14}$$

where C_i is the mass concentration of the component, ΔH_i is the enthalpy of components.

Energy is dissipated during phase change process, and heat flux due to phase change is

$$q_{\mathrm{phas}}=\sum m_i\int_{T_{-s}}^{T_s}c_i dT \tag{15}$$

where m_i is the mass of components occurring phase changes, c_i is the specific heat of corresponding components. In this paper, the phase change processes of the pyrolytic residual char and carbon fibers are mainly considered.

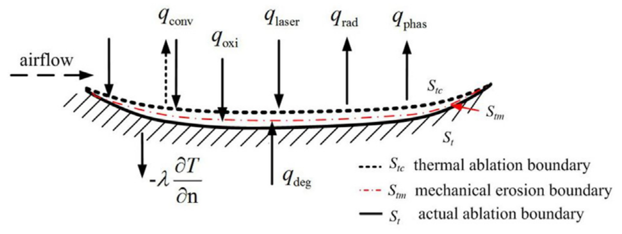

Fig. 8 – Heat transfer boundary conditions of laminated CFRP subjected to laser irradiation and tangential airflow.

3.4. Thermal ablation process and reaction heats

To model the thermal ablation behavior of CFRP, one needs to obtain the detailed ablation process and reaction heats. Thermal gravimetry (TG) and differential scanning calorimetry (DSC) tests in nitrogen environment and air environment at a heating rate of 25 °C/min were performed, as shown in Fig. 9. From Fig. 9a, three stages of thermal decomposition in a nitrogen environment can be identified: dehydration stage below 300 °C, pyrolysis stage of epoxy matrix from 300 to 700 °C, and sufficient decomposition stage above 700 °C. In the second stage, a clear mass-loss valley can be observed from DTG (differential of TG, by temperature). In contrast, complex behavior of thermal decomposition in an oxidation environment are observed, see Fig. 9b. There are several valleys and peaks in DSC curve, due to the endothermic reaction of pyrolysis and the exothermic reaction of oxidation, respectively. The exothermic reaction peak around 580 °C indicates residual char produced by pyrolysis epoxy is oxidized in the air. The peak around 823 °C attributes to the oxidation of carbon fibers.

Due to the limitation of TG tests, thermal decomposition of CFRP composites at higher temperature range and higher

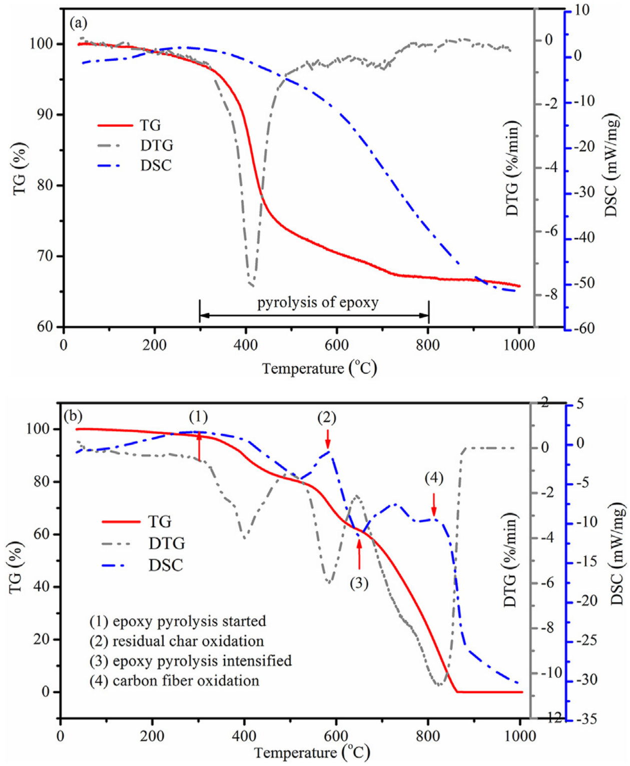

Fig. 9 – Thermal analysis of CFRP composites at different environments (a) nitrogen environment, (b) air environment.

heating rate that is comparable to laser irradiation is not available. According to Fig. 7, sublimation of carbon fibers occurred during the process of laser irradiation. As illustrated by [37], the temperature at which sublimation of carbon fibers occurred is set to 3300 °C. He et al. [37] carried out laser irradiation experiments on carbon fiber reinforced composites in the subsonic airflow environment. The research found that when the temperature of ablation zone reaches 3300 °C, carbon fibers produce sublimation. Therefore, the whole ablation process of CFRP composites is displayed in Table 3. It describes the details of series reactions and reaction materials, and this ablation process is helpful to build the numerical model.

Reaction heat of the pyrolysis and oxidation process needs to be calibrated by DSC results in Fig. 10 [38–40]. The endothermic heat Q during the degradation process, corresponding to the shadow region in DSC curve of nitrogen environment in Fig. 10, can be obtain by integration with respect of the baseline indicated in the figure, namely.

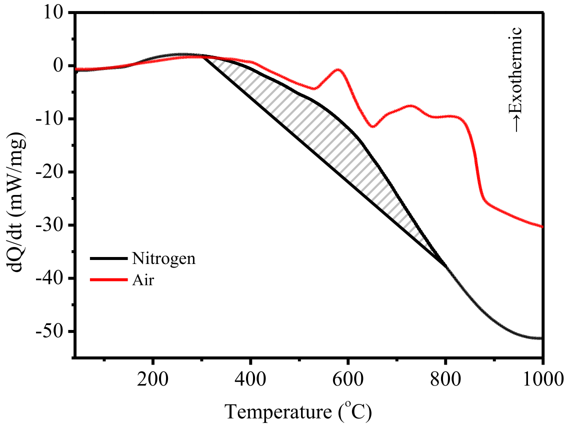

Fig. 10 – DSC analysis of CFRP in nitrogen and air environments to obtain pyrolysis heat and oxidation heat.

$$Q = \int_{t_1}^{t_2} \left(\frac{dQ}{dt} - BL \right) dt \tag{16}$$

where BL is the linear baseline temperature function. The calculated value of endothermic heat is −7.37 kJ/g, where minus sign stands for absorbing heat. Similarly, the exothermic heat by oxidation can be calculated by integration of the enclosed area between two DSC curves in air and nitrogen. Based on the DSC data, the value of exothermic heat is 20.9 kJ/g.

3.5. *Coupled thermal-fluid-solid analysis*

A coupled thermal-fluid-solid analysis integrating thermo-mechanical model in section 3.1 and linear ablation model in section 3.2 for CFRP is performed. The solver of computational fluid dynamics (CFD) and the solver of computational solid dynamics (CSD) are used to solve the partition problem independently, and coupling analysis is realized by controlling the data transfer on the fluid-solid boundary. In each time step, the boundary movement of each node caused by linear ablation is calculated by Eq. (4), and deformed meshes are adjusted by radial basis function (RBF). Iterative partitioned solution method needs to interleave solving each single field problem several times, until the equilibrium condition is satisfied, and then proceeds to the next time step calculation. Conservations and continuities of all physical quantities transferred at the fluid-solid interface (FSI) are strictly guaranteed, including temperature, heat flow and deformation. In a time step, the fluid field transfers the aerodynamic heat flow and

Table 3 – Thermochemical ablation processes of CFRP composites.

Time series	Temperature (°C)	Processes	Reaction material	Reaction heat (kJ/g)
T_0	20	Heating	Epoxy and carbon fibers	
T_1	300	Pyrolysis	Epoxy	−7.37
T_2	580	Oxidation	Residual char	20.9
T_3	823	Oxidation	Carbon fibers	
T_4	3300	Phase transition	Carbon fibers	

aerodynamic pressure through FSI to the structure field, and the structure field transfers the temperature and deformation through FSI to the fluid field.

There are some simplifications in the calculation, and only CAZ is considered. According to Fig. 6, most of the broken fibers are still attached to the test sample, therefore, mass loss in the DAZ is small. The ignorance of mechanical erosion effect in the DAZ in the simulation also dues to another two reasons. On the one hand, according to high-speed flow theory, the flow field in DAZ has no influence on the LAZ, i.e., it does not affect the ablation depth. On the other hand, this calculation is a coupled thermal-fluid-solid analysis, the mesh of flow field cannot be generated when CFRP is delaminated.

3.6. *Numerical results and discussions*

The numerical results are shown in the Figs. 11 and 12. And the initial parameters are given in Appendix A. Table 1A. Fig. 11a and b are the comparison of ablation profiles between numerical simulation and experimental result. Simulation results are in good agreement with experimental results. And Fig. 11c gives the ablation profiles on the center line of laser spot at different times. When the laser irradiation time (LIT) is between 0.8 and 2.4 s, the ablation depth significantly increases. When the LIT is more than 2.4 s, the ablation rate begins to decrease significantly. And the final ablation depth of the simulation is 1.296 mm, and the experimental result is 1.328 mm.

Fig. 12 gives the ablation depth of each ablation mechanisms at the center P_C and behind P_B (see Fig. 11c) of the ablation pit. As shown in Fig. 12a, the contribution of the sublimation to the total depth is the maximum and equal to 71% and the thermomechanical erosion is 29% when the LIT is shorter than 1.20 s. The matrix has been pyrolyzed and the pyrolytic carbon and fiber start to oxidize due to the heat conduction before the ablation pit degradation when LIT is between 1.20 and 2.24 s, and therefore the contribution of the oxidation increases to the 15.6–26.5%. The contribution of oxidation is decrease when the matrix pyrolysis is completed. When the LIT is 2.40 s, the contribution of the thermomechanical erosion decreases as a result of the significant decrease of the pressure head $p_{\sum}$. The total ablation depth is 1.296 mm, in which the sublimation depth is 0.704 mm, the oxidation depth is 0.278 mm and the themomechanical erosion depth is 0.314 mm.

Fig. 12b show the contribution of the thermomechanical erosion is 70.4% and the oxidation is 29.6% when the LIT is 1.2 s. The temperature of P_B is much lower than that of P_C (3000 K), the contribution of the sublimation is zero. When the

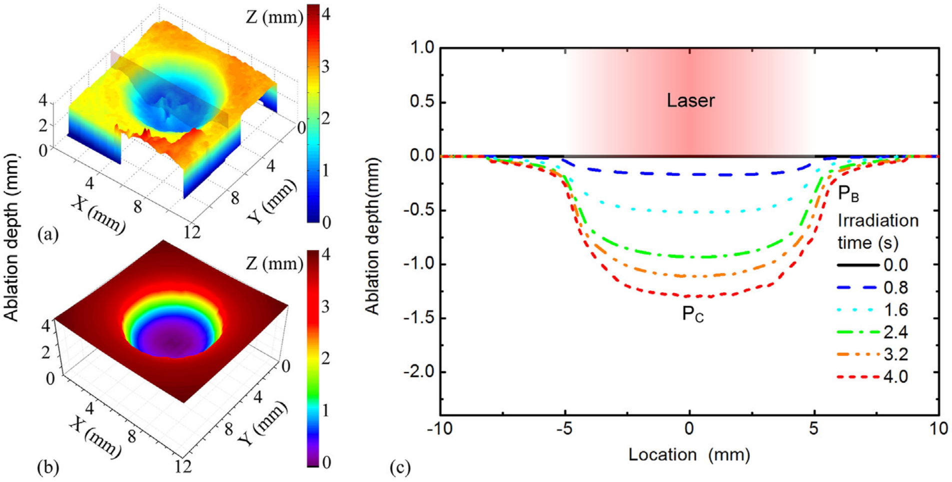

Fig. 11 – Laser ablation for 4 s at Ma 1.8 and 2000W (a) Experimental ablation morphology, (b) Numerical ablation morphology, (c) Comparison of cross-sectional ablation profile.

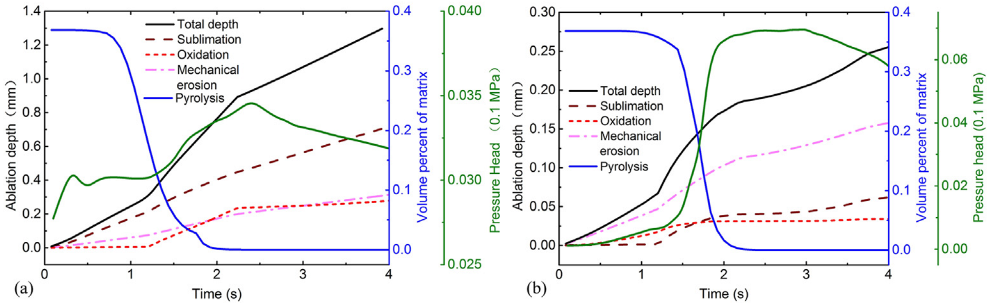

Fig. 12 – The effect of thermochemical ablation and thermomechanical erosion on laser ablation depth (a) P_C (The point of center), (b) P_B (The point of behind).

LIT is between 1.28 and 2.24 s, the ablation rate of the thermomechanical erosion increases with the increase of pressure head $p_{\sum}$. The pressure head of P_B is significantly larger, at least twice of the $P_{C.}$ The contribution of the thermomechanical erosion is dominant at the behind edge of laser pit. Finally, the total ablation depth of P_B is 0.255 mm, which is composed of the contribution of sublimation is 0.062 mm, the contribution of oxidation is 0.035 mm and the contribution of thermomechanical erosion is 0.158 mm.

4. Conclusions

The ablation behavior of laminated CFRP composite subject to high power laser irradiation in supersonic wind tunnel is investigated experimentally. The ablation rate increases with laser power density and Mach number. To compare the ablation behavior, laser ablation tests in 3 other environments are also carried out. It is found that the ablation rate of wind tunnel tests is at least twice that of the other conventional tests. This means, the thermomechanical erosion due to the tangential supersonic airflow play a significant role in the laser ablation process. The laser ablation rate increases in the order of static nitrogen, open airflow, static air, wind tunnel of Mach 1.8 and wind tunnel of Mach 3.0, when irradiated for 4 s by the same laser power density. Laser ablation mechanisms in supersonic wind tunnel tests can be classified into two categories, thermochemical effects and thermomechanical erosion. The former includes pyrolysis, oxidation and sublimation. The latter is a comprehensive effect due to the velocity of airflow, the pressure head of airflow, internal gas pressure and thermal expansion. Because of the different mechanisms, the ablation area can be divided into two regions: the coupled ablation zone (CAZ) and the downstream affected zone (DAZ). Although it seems that broken fiber caused by mechanical erosion is serious in DAZ, but this region has little influence on the ablation mass and the ablation depth. A coupled thermal-fluid-solid analysis revealed that the contribution of each laser mechanisms is distinctive at the different positions of the laser pit. The sublimation dominates the ablation depth at the center of laser pit, and it is equal to 54.32%. However, at the behind of laser pit, the contribution of the thermomechanical erosion is the maximum and equal to 61.96%.

Author contributions

Weina Zhao: Investigation Conducting, Data Curation, Writing-Original Draft.

Te Ma: Investigation Conducting, Software Programming, Writing-Original Draft.

Hongwei Song: Conceptualization, Supervision, Writing-Review & Editing, Project administration.

Wu Yuan: Investigation. **Lingling Lu**: Investigation. **Ruixing Wang**: Investigation. **Zhe Wang**: Investigation. **Chenguang Huang**: Conceptualization.

Declaration of Competing Interest

The authors declare that they have no known competing financial interests or personal relationships that could have appeared to influence the work reported in this paper.

Acknowledgement

Financial supports from National Natural Science Foundation of China (Grant Nos. 91016025, 11472276, 11332011 and National Defense Basic Scientific Research program of China No. JCKY2016130B009) are gratefully acknowledged. The authors would like to express their appreciation to Professor Yapu Zhao at the State Key Laboratory of Nonlinear Mechanics, Chinese Academy of Sciences, for providing 3D microscope apparatus to capture the ablation profile. The gratitude also goes to Professor Xinyu Zhang and Professor Hongbin Gu at the State Key Laboratory of High Temperature Gas Dynamics (LHD), Chinese Academy of Sciences, for providing and assisting the supersonic wind tunnel experiments.

Appendix A. The initial parameters of laminated CFRP

Table 1A – The input parameters in the coupled thermal-fluid-solid analysis.

No.	Symbol	Implication	Unit (mm)	Value
1	ρ_b	The density of matrix	$ton \cdot mm^{-3}$	1.2E-9
2	E_{Ab}	The activation energy of matrix	$mJ \cdot ton^{-1}$	1.75E5
3	J_{0b}	The pre-exponential factor of matrix	$ton \cdot mm^{-3} \cdot s^{-1}$	6E-6
4	ϕ_b^0	The concentration of matrix	None	0.97
5	k_{b0}	The conductivity of matrix	$mW \cdot mm^{-1} \cdot K^{-1}$	0.35
6	c_{pb0}	The specific heat of matrix	$mJ \cdot ton^{-1} \cdot K^{-1}$	1.2E9
7	ρ_p	The density of pyrolytic carbon	$ton \cdot mm^{-3}$	2E-9
8	ϕ_p^0	The concentration of pyrolytic carbon	None	0
9	k_{p0}	The conductivity of pyrolytic carbon	$mW \cdot mm^{-1} \cdot K^{-1}$	5
10	c_{pp0}	The specific heat of pyrolytic carbon	$mJ \cdot ton^{-1} \cdot K^{-1}$	6E8
11	Q_b	The reaction heat of the pyrolysis	$mJ \cdot ton^{-1}$	7.37E12
12	ρ_f	The density of carbon fiber	$ton \cdot mm^{-3}$	2.5E-9

(*continued on next page*)

Table 1A – (*continued*)

No.	Symbol	Implication	Unit (mm)	Value
13	E_{Af}	The activation energy of carbon fiber	$mJ \cdot ton^{-1}$	2E5
14	J_{0f}	The pre-exponential factor of carbon fiber	$ton \cdot mm^{-3} \cdot s^{-1}$	4.2E-6
15	$\mathit{\Gamma}_f$	The gasification coefficient of carbon fiber	None	0.1
16	ϕ_f^0	The concentration of carbon fiber	None	1
17	k_{b0}	The conductivity of carbon fiber	$mW \cdot mm^{-1} \cdot K^{-1}$	42
18	c_{pb0}	The specific heat of carbon fiber	$mJ \cdot ton^{-1} \cdot K^{-1}$	8.9E8
19	ρ_l	The density of crystalline phase	$ton \cdot mm^{-3}$	2.5E-11
20	ϕ_l^0	The concentration of crystalline phase	None	0
21	k_{l0}	The conductivity of crystalline phase	$mW \cdot mm^{-1} \cdot K^{-1}$	42
22	c_{pl0}	The specific heat of crystalline phase	$mJ \cdot ton^{-1} \cdot K^{-1}$	8.9E8
23	ϕ_{buc}^0	The initial volume percent of matrix	None	0.38
24	ϕ_{fuc}^0	The initial volume percent of carbon fiber	None	0.62
25	E_{AS}	The activation energy of the sublimation reaction	$mJ \cdot ton^{-1}$	2.04E5
27	A_i	The pre-exponential multiplier of the oxidation action	$ton \cdot mm^{-3} \cdot s^{-1}$	5E-10
28	E_{Ai}	The activation energy of the oxidation reaction	$mJ \cdot ton^{-1}$	2.51E4
31	J_f^0	The pre-exponential multiplier of the thermomechanical erosion	$ton \cdot mm^{-3} \cdot s^{-1}$	5.4E-10
33	σ_f, $\sigma_{f\perp}$	The strengths of carbon fiber in the longitudinal and perpendicular directions, respectively	MPa	2200, 220
34	E_{Aft}	The activation energy of the thermomechanical erosion	$mJ \cdot ton^{-1}$	5.82E4
35	n	the reaction order	None	3
36	γ	the ratio of specific heat	None	1.4

REFERENCES

[1] Chen Y, Ye L, Fu KK. Progressive failure of CFRP tubes reinforced with composite sandwich panels: numerical analysis and energy absorption. Compos Struct 2021;263:113674.

[2] Feng B, Ribeiro AL, Ramos HG. Interaction of Lamb waves with the edges of a delamination in CFRP composites and a reference-free localization method for delamination. Measurement 2018;122:424–31.

[3] Du ZC, Zhu MR, Wang ZG, Yang JG. Design and application of composite platform with extreme low thermal deformation for satellite. Compos Struct 2016;152:693–703.

[4] Li M, Chen L, Yang X. A feasibility study on high-power fiber laser cutting of thick CFRP laminates using single-pass strategy. Opt Laser Technol 2021;138:106889.

[5] Arabgol F, Kokabi M, Bahramian AR. Ablation behavior of organoclay-NBR insulator: modeling and experimental. Fire Mater 2018;42(7):859–72.

[6] Borrie D, Zhao XL, Raman RKS, Bai Y. Fatigue performance of CFRP patched pre-cracked steel plates after extreme environmental exposure. Compos Struct 2016;153:50–9.

[7] Nguyen PL, Vu XH, Ferrier E. Thermo-mechanical performance of Carbon Fiber Reinforced Polymer (CFRP), with and without fire protection material, under combined elevated temperature and mechanical loading conditions. Compos B Eng 2019;169:164–73.

[8] Li X, Hou W, Han B, Xu LF, Li ZW, Nan PY, et al. Thermal response during volumetric ablation of carbon fiber composites under a high intensity continuous laser irradiation. Surf Interfac 2021;23:101032.

[9] Wang S, Echeverr YJ, Trevisi L, Pranther K, Xiang LZ, Liu YT. Ultrahigh resolution pulsed laser-induced photoacoustic detection of multi-scale damage in CFRP composites. Appl Sci-Basel 2020;10(6):2106.

[10] Ferrante L, Tirillò J, Sarasini F, Touchard F, Ecault R, Vidal Urriza MA, et al. Behaviour of woven hybrid basalt-carbon/epoxy composites subjected to laser shock wave testing: preliminary results. Compos B Eng 2015;78:162–73.

[11] Gebauer J, Burkhardt M, Franke V, Lasagni AF. On the ablation behavior of carbon fiber-reinforced plastics during laser surface treatment using pulsed lasers. Materials 2020;13(24):5682.

[12] Kreling S, Fischer F, Delmdahl R, Gäbler F, Dilger K. Analytical characterization of CFRP laser treated by excimer laser radiation. Phys Procedia 2013;41:282–90.

[13] Leone C, Papa I, Tagliaferri F, Lopresto V. Investigation of CFRP laser milling using a 30 W Q-switched Yb:YAG fiber laser: effect of process parameters on removal mechanisms and HAZ formation. Compos Appl Sci 2013;55:129–42.

[14] Niino H, Harada Y, Fujisaki A. Thermal damage of carbon fiber reinforced plastic by IR fiber laser irradiation. J Laser Micro Nanoen 2017;12(3):235–8.

[15] Obunai K, Fukuta T, Ozaki K. Carbon fiber extraction from waste CFRP by microwave irradiation. Compos Appl Sci 2015;78:160–5.

[16] Stokes-Griffin CM, Compston P. Optical characterisation and modelling for oblique near-infrared laser heating of carbon fibre reinforced thermoplastic composites. Opt Laser Eng 2015;72:1–11.

[17] Allheily V, Lacroix F, Eichhorn A, Merlat L, L'Hostis G, Durand B. An experimental method to assess the thermo-mechanical damage of CFRP subjected to a highly energetic 1.07 mu m-wavelength laser irradiation. Compos Part B-Eng 2016;92:326–31.

[18] Dimitrienko YI. Thermomechanical behaviour of composites under local intense heating by irradiation. Compos Appl Sci 2000;31(6):591–8.

[19] Yongguang H, Shibing LIU, Lianchun L, Tian J, Zhiguang Y. Mass ablation characteristics of carbon fiber composite irradiated by Nd:YAG laser. Acta Mater Compos Sin 2009;26(1):118–22 [In Chinese].

[20] Tong YG, Bai SX, Hu YL, Liang XB, Ye YC, Qin QH. Laser ablation resistance and mechanism of Si-Zr alloyed melt infiltrated C/C-SiC composite. Ceram Int 2018;44(4):3692–8.

[21] Chippendale RD, Golosnoy IO, Lewin PL. Numerical modelling of thermal decomposition processes and associated damage in carbon fibre composites. J Phys D Appl Phys 2014;47(38).

[22] Mucha P, Berger P, Weber R, Speker N, Sommer B, Graf T. Calibrated heat flow model for the determination of different heat-affected zones in single-pass laser-cut CFRP using a cw CO2 laser. Appl Phys Mater 2015;118(4):1509–16.

[23] Wu CW, Wu XQ, Huang CG. Ablation behaviors of carbon reinforced polymer composites by laser of different operation modes. Opt Laser Technol 2015;73:23–8.
[24] Salama A, Li L, Mativenga P, Sabli A. High-power picosecond laser drilling/machining of carbon fibre-reinforced polymer (CFRP) composites. Appl Phys Mater 2016;122(2).
[25] Nan PY, Shen ZH, Han B, Ni XW. The influences of laminated structure on the ablation characteristics of carbon fiber composites under CW laser irradiation. Opt Laser Technol 2019;116:224–31.
[26] Farhan S, Ke-Zhi LI, Guo LJ, Gao QM, Lan FT. Effect of density and fibre orientation on the ablation behaviour of carbon-carbon composites. N Carbon Mater 2010;25(3):161–7.
[27] Zhang J, Ma Z, Feng G, He M, Liu W, Wei C. Influence of tangential airflows velocity on ablation heat of laser irradiated glass fiber reinforced resin composites. Chin J Lasers 2015;42(3):0306004 [In Chinese].
[28] Helber B, Turchi A, Scoggins JB, Hubin A, Magin TE. Experimental investigation of ablation and pyrolysis processes of carbon-phenolic ablators in atmospheric entry plasmas. Int J Heat Mass Tran 2016;100:810–24.
[29] Peng G, Zhang X, Gao Y, Yan H. Research to Mechanics erosion effect of laser irradiating glass/epoxy composites. Chin J Lasers 2015;42(1):0106001 [In Chinese].
[30] Lachaud J, Eekelen TV, Scoggins JB, Magin TE, Mansour NN. Detailed chemical equilibrium model for porous ablative materials. Int Heat Mass Tran 2015;90:1034–45.
[31] Lachaud J, Cozmuta I, Mansour NN, Vignoles GL, Aspa Y, Boyd ID, et al. Multiscale Approach to ablation modeling of phenolic impregnated carbon ablators. J Spacecraft Rockets 2010;47(6):910–21.
[32] Chippendale RD, Golosnoy IO, Lewin PL. Numerical modelling of thermal decomposition processes and associated damage in carbon fibre composites. J Phys D Appl Phys 2014;47(38):15.
[33] Sun Z, Li C, Ying T. Experimental and numerical investigations on damage accumulation and energy dissipation of patch-repaired CFRP laminates under repeated impacts. Mater Des 2021;201:109540.
[34] Ohkubo T, Sato Y, Matsunaga EI, Tsukamoto M. Three-dimensional numerical simulation during laser processing of CFRP. Appl Surf Sci 2017;417:104–7.
[35] Zhao W, Song H, Huang C, Huang Y. Modeling the failure behavior of CFRP laminates subjected to combined thermal and mechanical loadings. Int J Appl Mech 2017;9(3).
[36] Dimitrienko Y, Dimitrienko I. Effect of thermomechanical erosion on heterogeneous combustion of composite materials in high-speed flows. Combust Flame 2000;122(3):211–26.
[37] He J, Zhang L, Zhang Y, Tan F, Jin Y, Zhao J. The test of laser ablation of carbon fiber composites materials in airflow environment. Appl Laser 2014;34(2):118–21 [In Chinese].
[38] Zhu GL, Wang W, Wang R, Xiao YP, Yang YX, Dong A, et al. Thermal degradation behavior of resins in aluminium composite under isothermal condition. Polym Test 2017;61:448–54.
[39] Shi SB, Liang J, He RJ. Thermal decomposition behavior of silica-phenolic composite exposed to one-sided radiant heating. Polym Compos 2015;36(8):1557–64.
[40] Camacho N, May-Crespo JF, Rojas-Trigos JB, Martinez K, Marin E, Mondragon-Rodriguez GC. Thermal properties and degradation kinetics of epoxy-gamma-alumina and epoxy-zinc oxide lightweight composites. Rev Mexic Fisica 2020;66(4):479–89.